Materials & Design 212 (2021) 110256

Contents lists available at ScienceDirect

Materials & Design

journal homepage: www.elsevier.com/locate/matdes

On the use of multiple layer thicknesses within laser powder bed fusion and the effect on mechanical properties

Alex Gullane [a], James W. Murray [a], Christopher J. Hyde [a], Simon Sankare [b], Alper Evirgen [b], Adam T. Clare [a,*]

[a] Faculty of Engineering, University of Nottingham, Nottingham, UK
[b] Oerlikon AM GmbH, Feldkirchen, Germany

HIGHLIGHTS

- A method to produce single Laser Powder Bed Fusion parts containing multiple layer thickness regions in XYZ is presented.
- Throughput can be increased through use of coarse layer thicknesses, while maintaining part integrity using finer layers in selective volumes.
- Local part properties can be controlled through the design of interfaces between two disparate layer thicknesses.
- At present, interfacial porosity dominates failure at the layer thickness boundary.

GRAPHICAL ABSTRACT

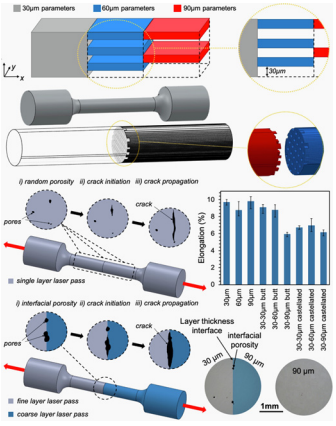

ARTICLE INFO

Article history:
Received 14 July 2021
Revised 9 November 2021
Accepted 15 November 2021
Available online 17 November 2021

Keywords:
Additive Manufacturing
Laser Powder Bed Fusion
Layer thickness
Tensile properties
Production rate
Local properties

ABSTRACT

Laser Powder Bed fusion is capable of rapid production of parts, from conception, compared with traditional manufacturing methods. This said, the time taken to fabricate a single part can still be significant – typically many hours. Processing thicker layers, and hence fewer total layers, in the Laser Powder Bed Fusion process, is an effective way to reduce build times. However, mechanical performance can suffer as a result of this strategy. This study proposes and demonstrates a method to enable the interlacing of multiple layer thicknesses within one part, allowing for finer layers within regions where they are specifically required, whilst maintaining overall component integrity for specific load cases. Thicker layers are used within regions with lower property requirements in order to optimise an overall part for improved production rate. The design of interfaces between two disparate layer thickness regions could also be tailored for control of material properties and such will be investigated in an independent study. Ti6Al4V LPBF samples are fabricated, characterised by way of tensile testing, porosity analysis and microstructural analysis. The study demonstrate parts can be additively built using multiple layer thickness regions with consistent ultimate tensile strength (1110–1135 MPa) and varying penalties to ductility, depending on layer thickness and interface design (elongation to failure reductions up to 40% in the most extreme case).

* Corresponding author.
E-mail address: adam.clare@nottingham.ac.uk (A.T. Clare).

https://doi.org/10.1016/j.matdes.2021.110256
0264-1275/

1. Introduction

Metal Additive Manufacturing (AM) techniques, such as Laser Powder Bed Fusion (LPBF), continue to gain industrial interest due to a number of unique benefits. Firstly, single-part design freedoms are possible that are not associated with traditional manufacturing methods, owing to the layer-by-layer nature of additive processes [1]. Example possibilities include internal cooling channels [2], lattice structures [3] and custom bone implants [4]. Secondly, significantly reduced material waste is possible, since near net shape components are achieved with little to no need for subtractive machining, while unprocessed powder feedstock can be recycled [5]. Also, in-process localised control of material properties can be introduced through the adaptation of build parameters [6], such as laser power, scan strategy, laser spot size, hatch spacing, scan speed, and beam focus.

Despite these benefits, a lack of confidence in the quality, consistency and mechanical integrity of build parts is preventing the wider adoption of LPBF in industrial applications. The LPBF process can produce parts with internal pores, and it is well understood that these internal defects can be responsible for initiating fracture under mechanical loading [7] (as found in this study). Such defects are particularly detrimental under cyclic loading [8], contributing to the poor repeatability exhibited by components built by LPBF. These internal defects fall into three categories: i) gas entrapment [9], in which pockets of air present in the powder feedstock are unable to escape the melt pool due to rapid cooling rates and hence small spherical pores remain within consolidated material, ii) keyhole pores [10], whereby recoil pressure allows molten material to travel upwards along the wall of a 'keyhole' during keyhole mode melting and seal over a large and misshapen cavity, and iii) lack of fusion [11], attributed to insufficient energy required to fuse successive layers as well as spatter particles [12], shielding the powder bed from the laser. Nonetheless, through optimisation of process parameters, scan strategy and use of high energy densities, near fully-dense components have been demonstrated in AM processable alloys such as Ti6Al4V [13].

Ti6Al4V is used within this study since it is a well-understood and relatively well-processed LPBF alloy. It was important to minimise risks in material processing since the primary focus was to investigate the process and not the material. Nonetheless, the method presented in this study is not material specific and may be performed with any LPBF processable alloy. While some LPBF components have been shown to produce greater strength than wrought counterparts [14], the typical as-built microstructure of LPBF Ti6Al4V (used in this study) yields both anisotropic grain structure and properties, as well as displaying ductility reductions up to 50% [15]. The microstructure comprises an α' martensitic phase contained within large columnar prior-β grains that grow epitaxially in the build direction [16] - upwards through the successive layers. A significant research effort has used post-build heat treatments to achieve increased ductility at the cost of a reduction in strength, aligning part performance closer to that of conventionally manufactured Ti6Al4V [17]. These treatments make use of temperatures below the β transus to decompose the α' martensitic phase in to α + β microstructure. Heat treatments below the β transus temperature, however, are not capable of changing the elongated prior- β grains responsible for anisotropy and poor fracture toughness, while those above the β-transus temperature capable of producing equiaxed β grains reported intolerable losses to strength and ductility [18]. Therefore, some limitations remain in part performance that may deter wider adoption of such techniques.

While AM is typically economical for one-off or small batch production, long build times limit the number of parts for which LPBF can be considered more productive than traditional methods [19]. Consequently, research exists adopting a number of methods to improve the throughput of the LPBF process. For example, Makoana et al. (2018) alter the process parameters to increase both laser power and spot size, increasing the energy density and size of the melt pool generated to form the part, allowing greater scan speeds and fewer passes to reduce build times [20]. However, increasing throughput in this manner involves tolerating penalties to mechanical performance and dimensional accuracy; this is counterintuitive to those adopting LPBF as a method to produce high performance parts. Alternatively, some studies have made use of commercially available LPBF machines featuring multiple lasers, that can simultaneously scan areas of the build bed with optimal parameters [21]. While this method achieves large build time reductions without the penalties to part quality, it is a very high-cost solution to rely on multiple laser optics systems within one machine.

Studies have shown Hot Isostatic Pressing (HIP) is effective in helping circumvent the sensitivity of the LPBF process to laser parameters for Ti6Al4V, by reducing internal defects [22] and reducing anisotropy inherent in the LPBF as-built microstructure [23]. Consequently, Herzog et al. (2020) achieved 25% build time reductions by simply operating greater scan speeds and relying on HIPing to remove the larger resultant porosity and maintain mechanical performance. Du Plessis et al. (2021) built on this, by producing hollow parts in which only the shell requires laser processing, and significant time is saved not scanning the volume [24]; HIPing is then used to consolidate the powder trapped internally and condense the shell to compensate for the void. This method achieved impressive part quality and build time reductions. The study exhibits a method to mitigate the effects of shell shrinkage on part geometry through finite element modelling, however, this method is limited to simpler geometries and must still be used in conjunction with laser processing to produce more complex parts associated with LPBF.

Increasing nominal layer thickness can reduce build times by discretising parts into fewer layers to process, significantly reducing the time required to complete a build and in turn increase throughput [25]. However, increasing layer thickness typically invokes penalties to part quality, including surface finish, dimensional accuracy and mechanical performance, due to larger grain sizes and an increased presence of porosity as the melt pool becomes less stable due to greater target penetration depths [26]. Many studies have demonstrated that larger layer thicknesses are an effective way to increase productivity, while failing to mitigate penalties to part performance. Nguyen et al. investigated layer thicknesses of 20, 30, 40 and 50 μm to identify trends in part quality of Inconel 718, showing that relative density, mechanical properties and dimensional accuracy were all superior in lower layer thicknesses [27]. Others have extended well beyond the normal process regime to achieve drastic productivity increases, such as 250 μm layers, for build time reductions in 316L parts [28]. 99.99% relative density was achieved with build rates of 9 mm^3/s; a 750% increase when compared with 1.2 mm^3/s build rates using 50 μm layer 316L samples [29] – using 400 W and 50 W lasers, respectively; hence greater energy density provided great benefit to the former. Despite observing superior relative density, the 250 μm layer components exhibited a significantly lower yield strength of 420 MPa when compared to 547 MPa reported by Yadroitsev et al. [29]. This further supports evidence that while thicker layers can increase throughput significantly, they yield penalties to mechanical performance, despite a lower volume of internal defects in this case.

A study by de Formanoir et al. proposed a method by which the core of a part is processed using fine layers to ensure part quality,

while the outer shell of the part comprises coarser layers – 30 μm and 90 μm layers respectively, termed a 'hull-bulk' strategy [30]. This is a sound example of how LPBF productivity can be improved, while maintaining part integrity, by assigning disparate layer thicknesses to select volumes within one part. However, the interface between layer thickness boundaries is not fully explored. For example, the study presented here explores further geometrical designs of interfaces (rather than planar) to improve fusion, as well as examining interfaces functioning within the bulk of parts, as opposed to only shells surrounding parts. This information is crucial for this method to be applied to a case study, in which crucial internal regions will require finer layers to withstand a given load case, while others can be formed with thicker layers to optimise production rate. A formative study of this research has previously been published [31], in which the principle of fabricating LPBF parts containing multiple layer thickness regions to increase throughput is demonstrated. However, excessive porosity meant samples failed well before reaching the plastic region and measuring interface design quality was not possible since all performed equally poorly. The present study investigates samples in which part parameters have been optimised to hugely reduce interfacial porosity and allow a full mechanical response to be observed, thus tensile properties and fracture surfaces can be used to compare interface design quality.

This study presents a novel method by which fine and coarse layer thicknesses can be interlaced into single LPBF parts, allowing for finer layers in regions of high specifications and coarse layers in regions of low interest or reduced mechanical requirements. This approach has several benefits. Firstly, it allows optimisation of parts for production rate by significantly reducing laser-on time, while maintaining part quality in the necessary areas. Secondly, it is a novel method to control property graduation, hence allowing control over fracture location and direction. Both 60 and 90 μm layers are interlaced with a benchmark 30 μm layer thickness, meaning these regions are only lased every second or third layer respectively. Flat and castellated interfaces are investigated. The castellated interface, featuring a grid arrangement of 'teeth' like a housing joint, is explored to improve fusion and exhibit the geometrical control enabled by this method. The quality of the union is characterised by porosity and microstructural analysis at the layer thickness boundary, and tensile testing of specimens featuring layer thickness interfaces within the gauge length are also performed.

2. Methodology

2.1. Specimen fabrication

The experimental work in this study investigates specimens produced using a commercial EOS M290 LPBF system. These samples were designed and tested to characterise fusion of disparate layer thickness regions, interlaced within a single geometry, with 30, 60 and 90 μm layer regions being joined together. In each case, optimised build parameters from the materials manufacturer were used to achieve near-fully dense consolidation of material (>99.9% relative density).

All specimens were produced using grade 5 Ti6Al4V feedstock, sourced from EOS, with a particle size distribution (PSD) of 20 – 63 μm. Samples were produced on an EOS M290 LPBF machine, at Oerlikon AM Europe GmbH in Feldkirchen, Germany. The system uses a continuous 400 W Yb-fibre laser with an 85 μm spot size and 250 × 250 × 325 mm build volume. Specimens were manufactured containing regions of 30, 60 and 90 μm layer thicknesses, each with an optimised parameter set produced by the manufacturer – corresponding volumetric energy densities (VED) can be found below in Table 1. Each region of a given part is sliced in EOSprint slicer software and discretised into the appropriate layer thickness and corresponding parameter set. Part regions were then arranged in the build volume within the software by inputting coordinates to ensure interfaces are perfectly aligned to form a 'single part', forming a cylinder lying horizontally on the substrate. The chamber conditions when processing parts were an oxygen content of 0.1% and platform temperature of < 45 °C. The samples were stress relieved at 720 °C for 2 h post-build in order to relieve residual stresses and improve ductility [18].

Table 1
Volumetric energy density required to consolidate nominal layer thicknesses of 30, 60 and 90 μm.

Layer Thickness (μm)	VED (J/mm^3)
30	55.6
60	37.8
90	27.8

Single parts were designed comprising two regions, one finer (30 μm) and one thicker layer (60 or 90 μm), to improve build rates through significantly reduced laser-on time. To achieve this, each region was designed separately in CAD software (SolidWorks, Dassault Systèmes, France) in order to slice the STL files at different nominal layer thicknesses using the optimised parameters in each case. Once sliced, the build files were aligned on the substrate within the slicer software to form one component comprised of two distinct regions. For this method to print successfully, increased layer thickness regions must be divisible by the base layer thickness – in this case 60 and 90 μm, divisible by the 30 μm baseline – since the build is performed at the finest thickness and thicker layers are processed every second and third layer respectively. This method is depicted in Fig. 1, along with the two joint geometries designed and fabricated within the study.

If half (or any appropriate fraction) of each sample is only lased every third layer, build times can be reduced significantly. Naturally, the amount of time saved is dependent on the size of the build. For example, take a build with the following parameters: 100 mm z-height + 5 mm support = 105 mm; 30 μm layers = 3500 layers; 30 s average laser-on time per layer; coarse layer scan speed 20% slower than fine layer scan speed. This means on layers where both halves are processed, the fine-layer region contributes 0.5 of the laser on time, while the coarse layer region contributes 0.6 of the laser on time compared to conventional processing. This equates to a time saving of 8hrs45mins or 22.5% build time reduction, accounting for 10 s recoater time per layer.

A series of cylindrical dog bone specimens were produced for tensile testing according to ASTM E8M 16a, with 24 mm and 4 mm gauge length and diameter respectively. 10 mm diameter grip sections were maintained from the standard. These were machined from blanks built as described above. Images of blanks, tensile specimens and specimen dimensions are shown in Fig. 2. ASTM E8M 16a defines a series of standard specimen geometries for room temperature tensile testing; of which, the stated 'reduced size' geometry was deemed appropriate for AM samples to maximise the usage of the build envelope as well as material usage. Similarly, cubic specimens were manufactured with identical joint interfaces, for image analysis. The samples consist of 9 sample sets. As a baseline, single layer-thickness 30, 60 and 90 μm dog bones were produced (with no joints to serve as a comparison for the specimens that feature disparate layer thickness interfaces). Then two interface geometries were investigated; a flat joint much like a butt joint, and a castellated joint, interlacing the two regions to improve the weld region. Samples were manufactured exhibiting 30–30 μm, 30–60 μm and 30–90 μm layer interfaces using both

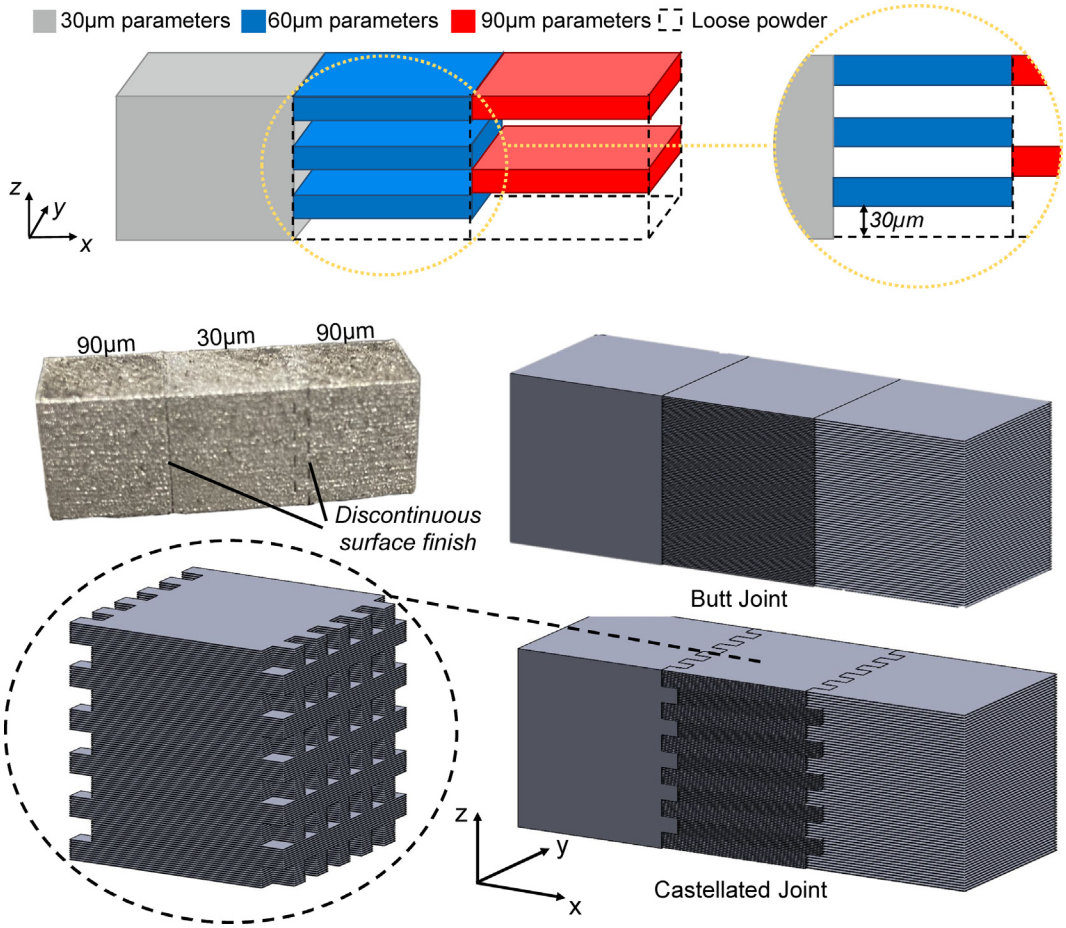

Fig. 1. A schematic showing the method by which multiple layer thicknesses can be interlaced within single LPBF geometries (top); CAD images of the two jointed geometries investigated as part of the study (butt and castellated joints) [31]

joint types, thus forming the nine sample sets along with the baseline specimens.

2.2. Microstructural analysis

Cubic samples, including the joint configurations described above, were sectioned in both the x-z and x-y planes (*see* Fig. 1 for cartesian axes with respect to build process) to observe interfacial porosity and blending of microstructure at the layer thickness interface. Samples were sectioned using abrasive cutting, and prepared via mechanical grinding followed by mechanical polishing down to colloidal silica. Samples were then imaged for porosity using a Nikon eclipse LV100ND optical microscope at 5-times magnification, prior to etching to avoid altering pore size and morphology by eroding pore boundaries with the etchant. Porosity analysis at the layer thickness boundary was necessary to understand whether this method of manufacture introduces defects at the interface and to correlate this information to the tensile results. ImageJ software was used to measure relative density across various 2 × 2 mm areas within each image and take an average reading in bulk regions compared to interface regions. Once porosity images were collected, the samples were then etched using Keller's reagent to reveal grain boundaries and imaged a second time on the optical microscope for analysis of the grain structure at the layer thickness boundary. While the 30–30 µm jointed samples will contain the same structure in each region, these samples were manufactured to determine whether the introduction of a joint gives rise to other features in the material, potentially weakening the specimens, be it through interfacial porosity or a microstructural phenomenon brought about by parallel laser scans. In the case of 30–60 and 30–90 µm joints, one expected to observe similar large columnar prior- β grains in the build direction (z-direction)[32]. The microstructural analysis presented in this study aimed to observe the blending of two disparate grain structures across the joint interface, and whether the joint geometry could improve said blending. The castellated joint geometry features 900 µm teeth in an attempt to broaden the region of blending and improve the fusion by interlacing the two layer thickness regions.

2.3. Tensile testing and fractography

Following the investigation of the quality and fusion of parts containing two disparate regions, the subsequent mechanical response is of primary concern. Tensile testing was selected as an indicative and time effective method of characterising this mechanical performance of jointed samples, compared to baseline single-layer-thickness samples (those presented here and those found in the wealth of information surrounding tensile properties of LPBF Ti6Al4V in the literature [333435]. Three repeats were performed for each sample set to ensure reliability in the data and observe repeatability across the sample sets. The samples were uniaxially loaded on a standard tensile test system with a crosshead translation speed of 1 mm/min until specimen failure, using a video extensometer to measure the stress–strain response. All specimens failed within the gauge length.

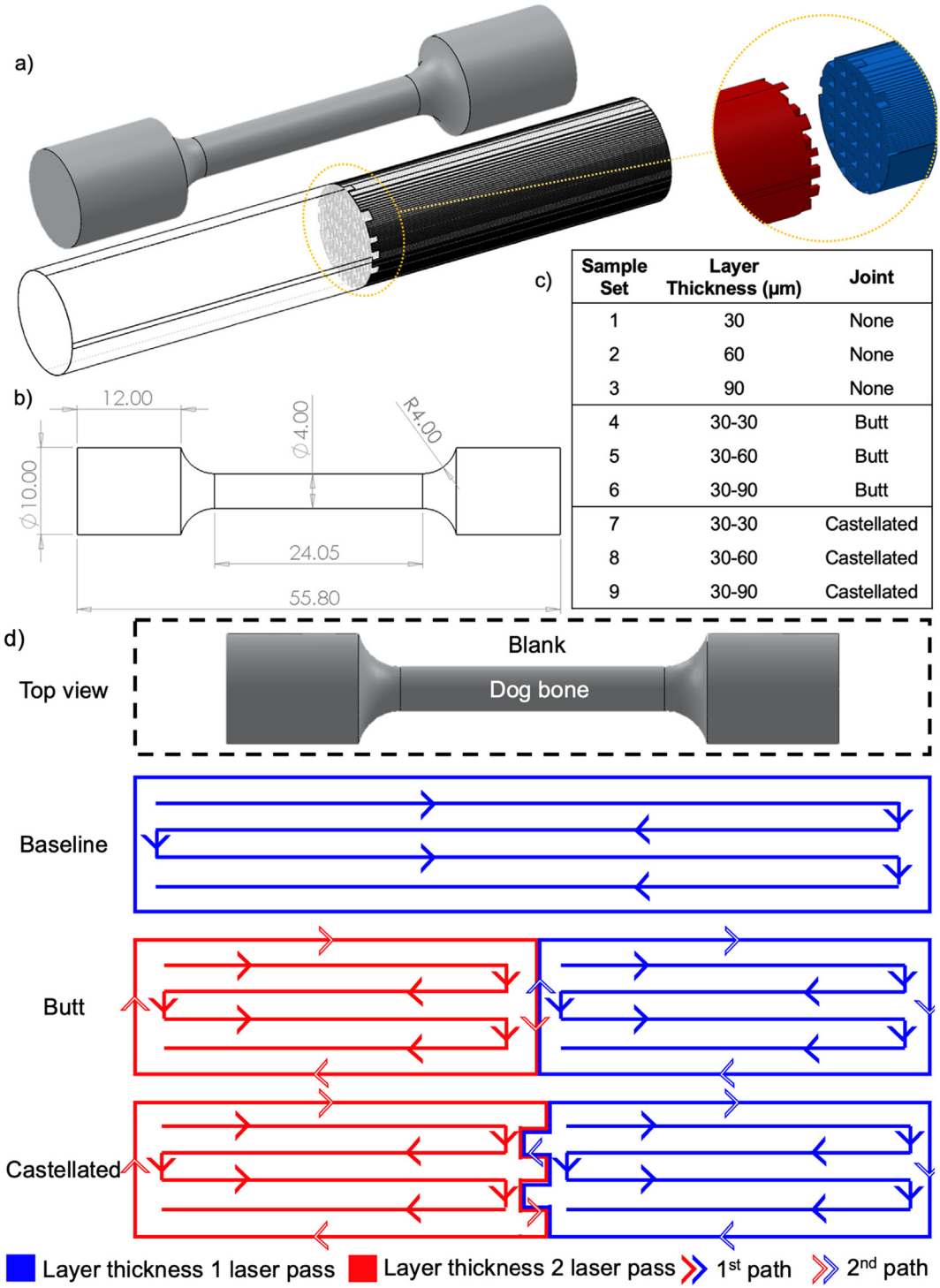

Sample Set	Layer Thickness (μm)	Joint
1	30	None
2	60	None
3	90	None
4	30-30	Butt
5	30-60	Butt
6	30-90	Butt
7	30-30	Castellated
8	30-60	Castellated
9	30-90	Castellated

Fig. 2. a) CAD images of Ti6Al4V LPBF blanks featuring a castellated union of two regions built with different layer thicknesses and the final machined tensile specimens; b) dog bone dimensions according to ASTM E8M 16a; c) a table describing the nine sample sets investigated in terms of layer thickness and joint configuration; d) schematics to describe laser processing of the samples.

Following tensile testing, failed sample fracture surfaces were analysed using an Alicona 'Infinite Focus' focus variation microscope (FVM) at 10x magnification and post-processed using Mountains surface metrology software. Fracture surfaces were investigated for a number of reasons i) to observe the fracture behaviour in terms of ductility, since introduction of layer thickness boundaries has potential to cause more brittle failure at the interface ii) to observe whether joint geometry relates to crack initiation and propagation, such as evidence of castellated teeth iii) to deduce whether samples failed at the joint interface, and hence determine whether interfaces introduce weak points in the parts and iv) to obtain supporting information as to why a sample may fail at the interface (e.g. internal defects). This information is used in conjunction with micrographs and tensile data to gain a deeper

insight into the behaviour of parts containing interlaced layer thicknesses, and to understand why they may fail in the manner observed here.

3. Results

3.1. Porosity and grain structure

Optical micrographs of 30–30, 30–60 and 30–90 μm interfaces for both butt and castellated joined regions are presented both prior to and post etching to observe porosity and grain structure, respectively. Evidence of defects at the interface provides crucial information as to the quality of the fusion between the two regions of different layer thicknesses, and useful insight in to fracture locations of the tensile specimens. Grain structure analysis allows investigation of the blending of two parallel laser scans, producing two metal matrices that form one part.

Imaging revealed an increase in porosity at the joint interfaces as opposed to the bulk regions, both in terms of frequency and size – highlighted in the micrographs in Fig. 3. This finding suggests a phenomenon occurs during laser processing of two parallel scan paths that introduces defects otherwise not present in a single layer thickness, single meander laser pass. A trend is clear from the relative density data as well as visual inspection of the images (Fig. 4), that an increase in layer thickness in the coarser layer region amplifies the increase in frequency and size of interfacial defects. The bulk regions of 30, 60 and 90 μm measured 99.99, 99.99 and 99.98% relative densities respectively, while joining these regions with a 30 μm region and measuring at the interface gives 99.92, 99.88 and 99.77% respectively.

Across all samples, micrographs display typical prior- β grains that appear elongated in the xz-plane and equiaxed in the xy-plane as seem from Fig. 5.This means columnar grain growth is evident in the build direction (z direction), as is typical in LPBF Ti6Al4V [36] (*see* Fig. 5). The microstructure observed in the 30–30 and 30–60 μm samples is very similar and can be seen to share grains across the boundary interface that match the general size, morphology and direction of the remainder of the sample. This provides some insight that good fusion occurs across the interface, that did not significantly disrupt the grain growth of each region, but rather blended the two together. This is not the case for the 30–90 μm samples, in which there is a clear band at the boundary of the butt jointed samples and in which texture of the grains has been affected. Some finer horizontal grains can be seen to grow outward from the interface line into the bulk of each region either side.

Another identified phenomenon is a change in directionality of the columnar grains across the interface, observed in the xy-plane and evident only in the 30–60 and 30–90 μm samples – the 30–30 μm samples show a consistent directionality across the whole surface. Observed from the xz-plane, the columns appear unchanged and aligned vertically in the build direction. However, the xy-plane reveals disparate angles in the alignment of the cross section of the columnar grains when comparing the two regions each side of the interface. The samples showed an angle disparity across the interface of 3.9, 35 and 23.1° for the 30–30, 30–60 and 30–90 μm samples respectively.

3.2. Tensile properties

Stress–strain curves and tabulated data are presented for baseline 30, 60 and 90 μm samples as well as 30–30, 30–60 and 30–90 μm samples featuring both butt and castellated joints between regions. As shown in the tensile response displayed in Fig. 6, repeatability of the samples is good for AM parts, owing to two factors. Firstly, a very high relative density and hence lack of internal defects that would give rise to less consistent failure; secondly, robust melt pool control producing consistent grain size. Consequently, the scatter among repeats is difficult to discern. In addition, the tensile response of the 30, 60 and 90 μm baseline specimens are indistinguishable. As a result, a second set of graphs (Fig. 7) has been included, in which the stress range depicted on the y-axes is magnified from 1200 to 80 MPa to focus on the plastic region, in which ultimate tensile stress and fracture point is observed.

All tested samples exhibited failure within the gauge section. In the case of the baseline 30, 60 and 90 μm samples, fracture occurred at random points along the gauge. In the case of all jointed samples (30–30, 30–60 and 30–90 μm, butt and castellated), fracture occurred at the midpoint of the gauge - the location of the interface between the two regions.

Fig. 7 (a) shows minor disparity amongst the tensile response of the baseline samples, showing an average UTS of 1126, 1131 and 1129 MPa for 30, 60 and 90 μm layer thicknesses respectively. There is no apparent trend in the baseline samples, and these minor changes (<0.5%) can be attributed to wider manufacturing tolerances associated with AM techniques. Elastic modulus (calculated from the gradient of the elastic region in the stress–strain graph), elongation to failure, strength and yield stress can also be considered comparable in each case – *see* Table 2.

This is explained by sound parameter optimisation and process control. It is clear from the graph that the 30 μm and two 30–30 μm jointed samples exhibit similar Young's modulus and UTS values - confirmed in Table 2 to range between 127.8 and 133.8 GPa and 1122–1130 MPa respectively for the three sample sets. However, while the butt jointed 30–30 μm samples perform very similarly to the standard 30 μm samples in terms of elongation (9.07% and

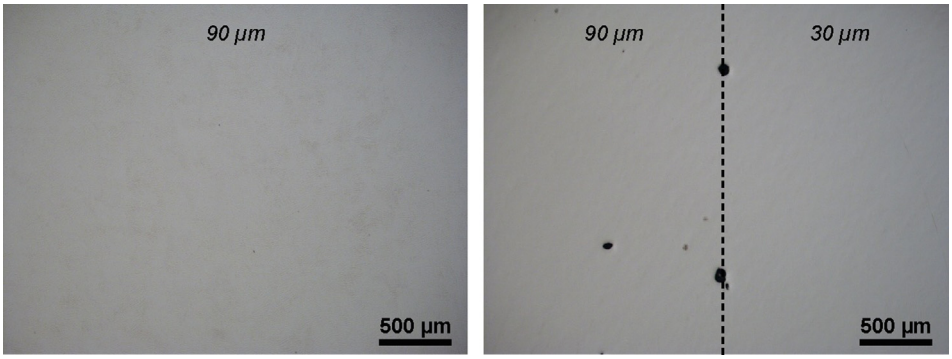

Fig. 3. 90 μm layer thickness bulk porosity compared with porosity at a 30–90 μm layer thickness interface, highlighting the increased presence in the region of interfaces.

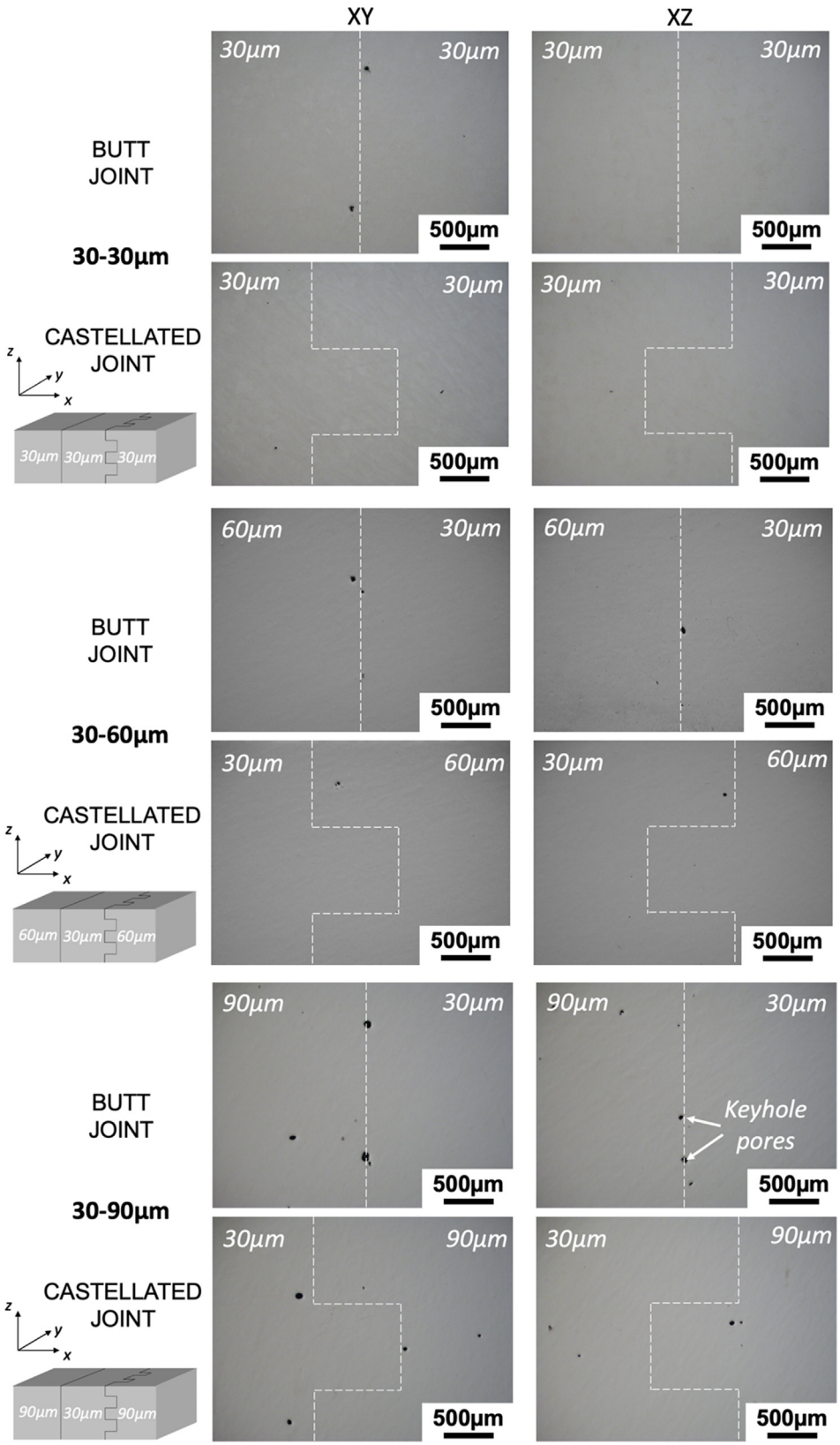

Fig. 4. Optical micrographs showing porosity at layer thickness interfaces in the xy plane (left column) and xz plane (right column) for butt joint and castellated joint boundaries; 30–30 μm regions (top rows), 30–60 μm regions (middle rows) and 30–90 μm regions (bottom rows); images depict an increase in defect presence and size at the interfaces, the extremity of which increases as layer thickness increases.

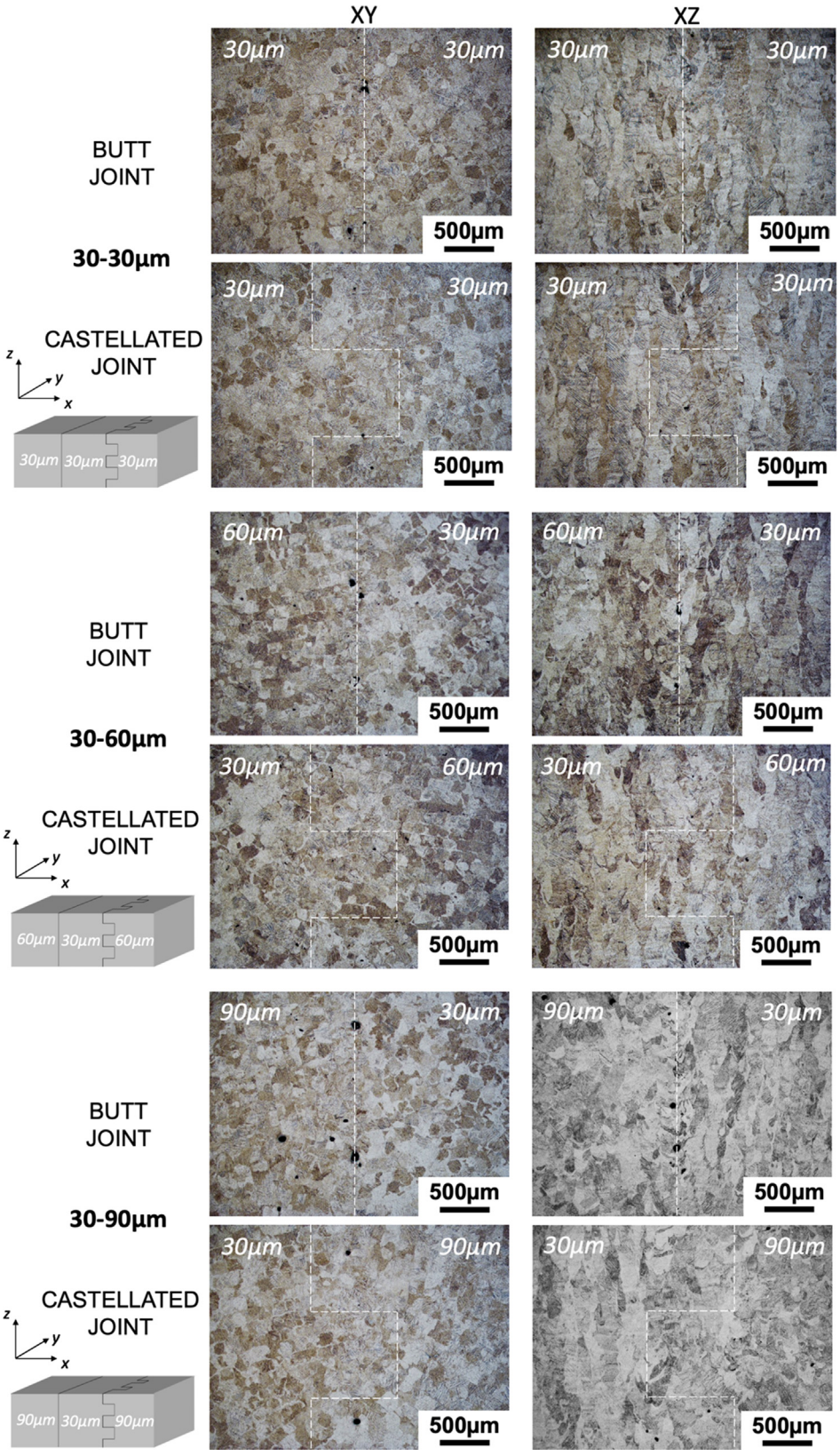

Fig. 5. Optical micrographs showing grain structure at layer thickness interfaces in the xy plane (left column) and xz plane (right column) for butt joint and castellated joint boundaries; 30–30 μm regions (top rows), 30–60 μm regions (middle rows) and 30–90 μm regions (bottom rows).

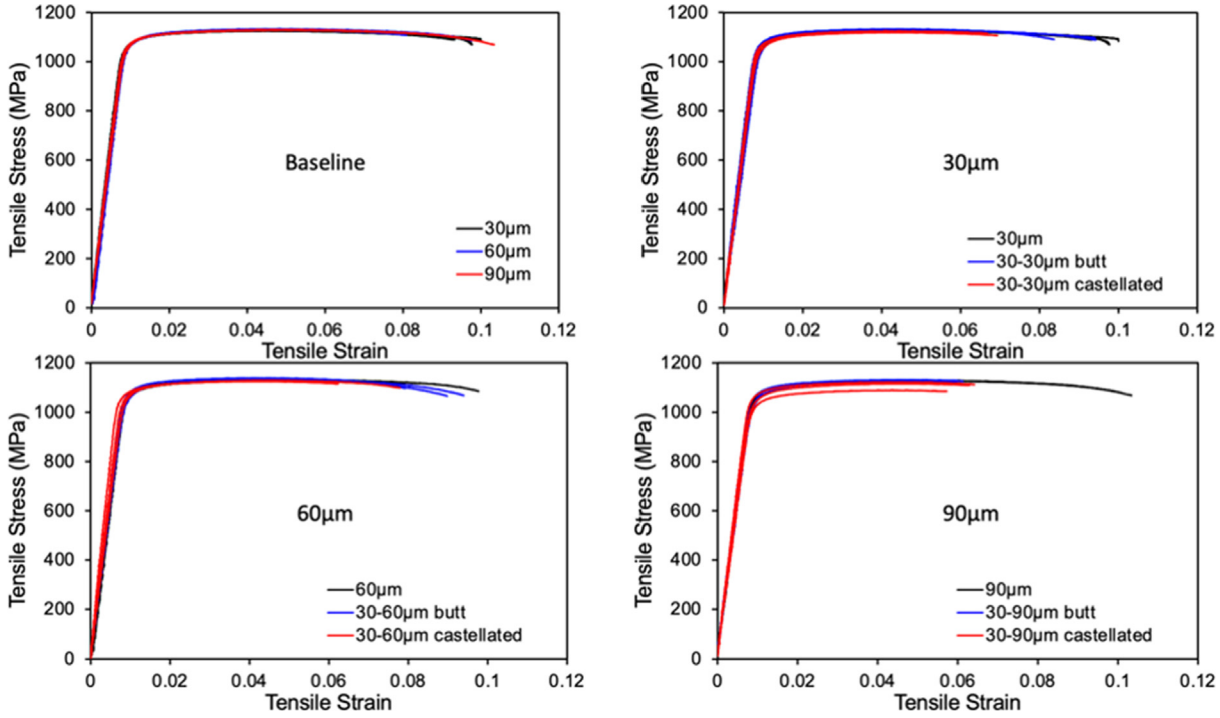

Fig. 6. Stress–strain curves displaying the tensile response of reduced-size, cylindrical dog bone specimens, manufactured by LPBF from Ti6Al4V feedstock and featuring disparate layer thickness interfaces at the gauge-length midpoint; top-left graph displays the baseline tensile responses of single layer thickness samples of 30, 60 and 90 µm layers; top-right graph displays 30–30 µm butt and castellated joint samples compared with the 30 µm baseline; bottom-left displays 30–60 µm butt and castellated joint samples compared with the 60 µm baseline; bottom-right displays 30–90 µm butt and castellated joint samples compared with the 90 µm baseline.

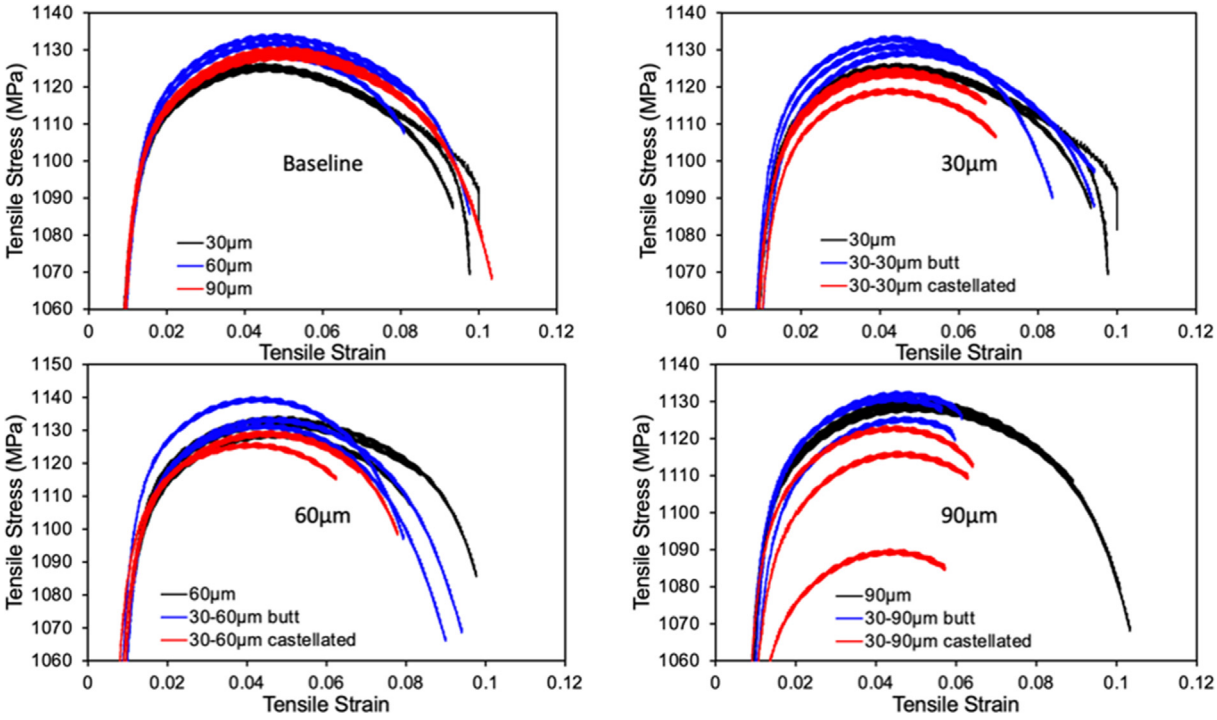

Fig. 7. Identical graphs and layout to Fig. 5, refining the y axes over an 80 MPa range to better visualise data scatter.

9.70% respectively), the castellated 30–30 µm joints exhibit failure at 6.71% elongation.

The bottom-left graphs in Fig. 6 and Fig. 7 depict the performance of the 30–60 µm jointed samples compared with the baseline 60 µm layer thickness. The trend is comparable to the 30–30 µm joints, in that the butt jointed samples perform very similar to the baseline samples; while the castellated joints, however, experience failure at 6.94% elongation compared with 8.74% and 8.78% for 60 µm baseline and 30–60 µm butt joints respectively. The blending of microstructure across the interface in these sam-

Table 2
Tensile properties of interlaced layer thickness Ti6Al4V parts produced by LPBF, including Young's modulus, elongation, UTS and yield stress; a comparison from literature and to wrought Ti6Al4V with similar heat treatments is included at the bottom of the table.

Sample Set	Elastic modulus (GPa)	Avg. elongation (%)	Avg. UTS (MPa)	Avg. Yield Stress (MPa)
30 μm	133.8 ± 1.01	9.70 ± 0.34	1126 ± 0.32	1071 ± 2.12
60 μm	129.1 ± 3.07	8.74 ± 0.90	1131 ± 2.54	1072 ± 4.30
90 μm	128.6 ± 3.82	9.78 ± 0.76	1129 ± 1.04	1074 ± 1.01
30–30 μm butt	127.8 ± 9.28	9.07 ± 0.61	1130 ± 1.95	1074 ± 3.89
30–60 μm butt	127.5 ± 2.66	8.78 ± 0.75	1135 ± 4.19	1074 ± 9.01
30–90 μm butt	124.2 ± 6.77	5.92 ± 0.25	1129 ± 3.68	1067 ± 8.83
30–30 μm castellated	130.4 ± 4.81	6.71 ± 0.22	1122 ± 2.98	1067 ± 4.85
30–60 μm castellated	140.9 ± 11.93	6.94 ± 0.78	1128 ± 1.94	1071 ± 0.57
30–90 μm castellated	127.0 ± 8.20	6.15 ± 0.37	1110 ± 17.6	1052 ± 16.2
Wrought Ti6Al4V [37]	113.8	14	950	880
LPBF Ti6Al4V [38]	94.4 – 110.9	2 – 19.7	840–1320	974

ples has been shown to be good in section 3.1.2, with the only difference to the 30–30 jointed samples being a change in directionality observed in the xy-plane between the two regions (the angle of grain alignment differs). Since the performance of the 30–60 μm jointed samples appears very similar to the 30–30 μm counterparts, it would suggest this change in directionality does not affect the tensile performance when loaded in the y-direction as in this study.

Fig. 7 (d) shows the samples with the largest disparity in layer thickness – the 30–90 μm jointed samples. The butt jointed samples, in this instance, give a similar Young's modulus, UTS and yield stress to the baseline samples; however, these specimens are the only butt jointed tests to yield premature failure and hence lower ductility in line with the castellated samples – dropping from the region of 9% elongation to failure to 5.92%. The 30–90 μm castellated samples again show premature failure and a reduction in ductility to the same extent as the 30–30 and 30–60 μm castellated interfaces. These are the first samples, however, to begin to show any depreciation in UTS and yield stress, as well as elongation (Young's modulus remains consistent). There is a marginal drop of around 1.4 and 1.6% in average UTS and yield stress respectively; while this is a very minor change, it is the first sign of any influence on stress response.

3.3. Fracture behaviour

Since the sample sets investigated are comprised of interfaces at the midpoint of the gauge, in two geometrical variations and three combinations of layer thickness (butt and castellated joints featuring 30, 60 and 90 μm regions), the fracture locations and surfaces were investigated. The baseline samples, Fig. 8 (a), (b) and (c), all failed at random points within the gauge length. This was expected due to the singular laser scan path producing a consistent grain structure and random porosity throughout the entire sample. The jointed samples, including butt joints and castellated joints featured in Fig. 8 (d, e, f and g, h, i respectively), all fractured at the midpoint of the gauge where the joint interfaces are situated.

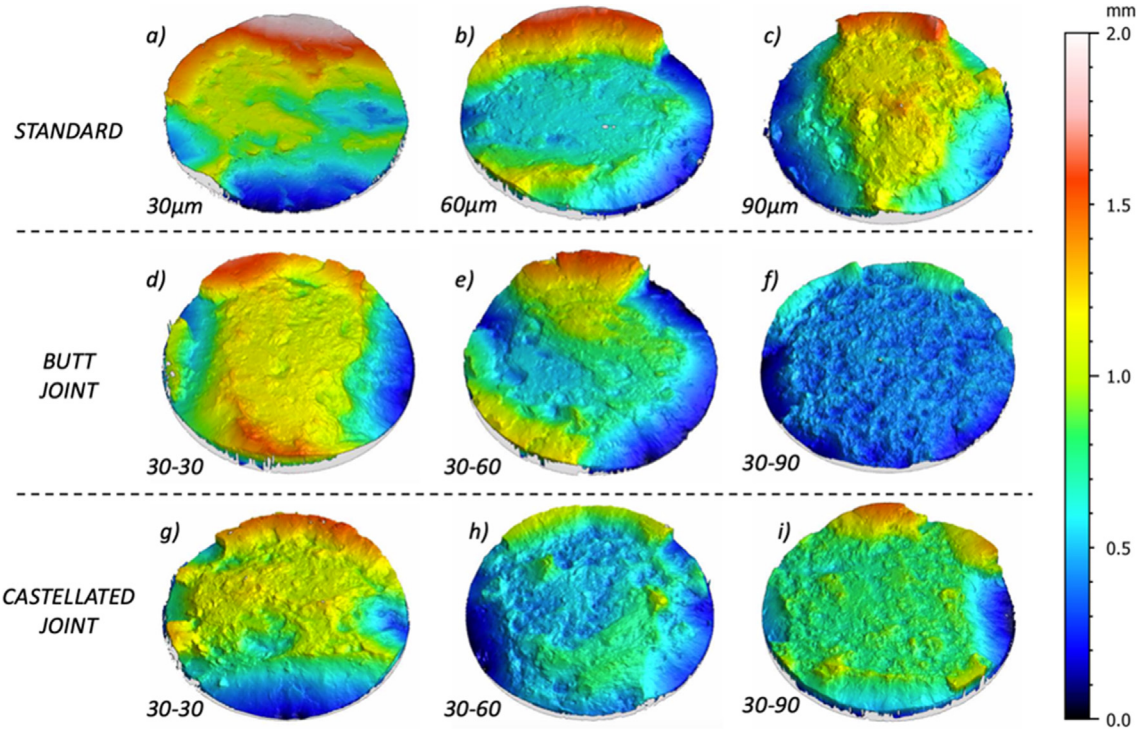

Fig. 8. Focus variation images of the fracture surfaces introduced when tensile testing the interlaced layer thickness LPBF specimens to failure; top row (a, b and c) includes baseline samples of singular layer thicknesses 30, 60 and 90 μm respectively; middle row (d, e and f) includes butt jointed layer thickness regions of 30–30, 30–60 and 30–90 μm respectively; bottom row (g, h and i) includes castellated joints between layer thickness regions of 30–30, 30–60, and 30–90 μm respectively.

The baseline samples all exhibit a standard cup and cone fracture surface, in which the high lips (red) and low recesses (blue) indicate the moderate ductility reported in the tensile results. The rougher texture displayed in the 90 μm surface (top-right in Fig. 8) is indicative of lower structural homogeneity brought about as a result of greater porosity within the sample, and thus yields a greater number of localised peaks and recesses, or 'dimples' – similar evidence was reported by Khalid Rafi et al. in 15–5 PH steel [39]. Despite this evidence, the 90 μm sample performed similarly with both the 30 and 60 μm samples under tension.

The butt jointed samples (Fig. 8d, e and f) show the inverse relationship between layer thickness and ductility found in the tensile data. The 30–30 μm joint maintains the lips and recesses around the perimeter, characteristic of a ductile cup and cone fracture; this is less apparent in the 30–60, and the 30–90 joint shows very little evidence of ductility, implying the more brittle, premature failure reported in the mechanical data as a consequence of interfacial porosity. The rougher texture and dimples observed in the 30–30 μm butt joint fracture surface when compared with the baseline 30 μm surface suggests a greater presence of pores, each dimple representing localised brittle behaviour in the vicinity of a pore. This strongly supports the hypothesis that the jointed samples fail at the layer thickness boundary as a result of interfacial porosity. Nonetheless, the fracture surface of this sample implies superior material uniformity and load sharing capability when compared with all other jointed samples, as was supported by showing the least interfacial porosity and strongest grain blending at the boundary in the microstructural analysis.

In agreement with the mechanical data, more brittle failure is evident across the board for the 30–30, 30–60 and 30–90 μm castellated samples; less evidence of standard cup and cone failure is apparent since little deformation was achieved prior to failure. Dimples are evident in all three surfaces again, further supporting the theory that interfacial porosity is the root cause of fracture occurring at the interface, as well as causing premature failure of the sample.

4. Discussion

4.1. Porosity and grain structure

The results suggest that producing LPBF parts comprising of different layer thickness regions gives rise to increased porosity (size and frequency) at the boundary. A trend is also evident in which increasing the thickness of the coarser layer region increases the extent of interfacial porosity. This trend can likely be attributed to two factors. Firstly, keyhole pores are increasingly more evident in LPBF parts as layer thickness increases, since melt pool stability becomes more difficult to maintain at greater depths of penetration. Thus, an increase in layer thickness in one or both regions is likely to give rise to a greater fraction of larger defects; especially since the border laser pass for each region is shared at the interface, and hence will be scanned twice over at a greater energy density input. Moreover, greater porosity exists at the interface in larger layer-thickness builds than exists in the bulk 60 and 90 μm regions, hence the introduction of a joint must be responsible for the presence of these interfacial pores. The trend also implies an increase in the coarse region layer-thickness increases the extent to which interfacial pores occur. The second contributing factor is thought to be the timing with which the two regions are processed. Since the 60 and 90 μm regions are only lased every second or third layer respectively, while the 30 μm regions are lased every layer, one can expect a vertical wall of consolidated material against loose powder at the interface. For example, in layers where both a 30 μm and 90 μm layer region is processed, there exists a 60 μm consolidated region bordering 60 μm of loose powder beneath – where two 30 μm layers were processed, but the 90 μm layer is yet to be processed. This means when the border laser pass for the 60 or 90 μm regions is processed, a workpiece consisting of half consolidated material is produced (with near fully dense material) and half loose powder with a 65% packing density. The two are expected to exhibit significantly different laser absorptivities, with loose powder yielding superior energy absorption owing to the reflectivity of spherical Ti6Al4V powder particles enhancing laser irradiation [4041]. It is possible, then, that the increased presence of keyhole pores can be attributed to a consistent remelting of previously consolidated material, since each 60 or 90 μm layer will require processing both a part-solid and part-loose-powder vertical interface below the current 30 μm layer being processed (one or two 30 μm layer region/s having been consolidated, and a loose powder 60 or 90 μm layer region). The parameters used to manufacture the specimens were optimised for consolidation of a uniform powder bed, hence further work modelling melt conditions at disparate layer-thickness interfaces (in which the powder bed is non-uniform) would likely inform methods to reduce interfacial porosity. Alternatively, custom scan paths can be explored to process each region as one continuous part to remove this phenomenon.

The presence of these larger pores aligned along the layer thickness interface is important, since it likely dictates both the fracture location and direction. In excess, this has potential to cause premature failure and hence lower ductility when compared with a single layer thickness, single region part, since keyhole pores accelerate crack initiation and propagation – *see* Fig. 9. This was confirmed by the tensile results and discussed in section 4.2.

The micrographs in Fig. 5 show a band of fine grains growing out horizontally from the interface of the 30–90 μm butt jointed samples. This can likely be attributed to the remelting required of 90 μm layers. Since more time has passed to allow the previous two 30 μm layers to solidify, heat flux flows horizontally from the 90 μm layer of loose powder in to the 60 μm solid wall (plus 30 μm loose powder above) and encourages horizontal grain growth in the opposite direction. These finer horizontal grains are not evident in the castellated joint samples, possibly owing to the geometry of the teeth preventing a consistent vertical wall as it shifts 900 μm periodically. Apparent instead, is a clear arced interface in the microstructure that highlights a harsher boundary between the two metal matrices (highlighted in Fig. 5l), suggesting blending of the two is poor among these samples.

Another change observed in the micrographs is a change in alignment of the columnar grains. This was shown to have no bearing on the mechanical response and is attributed to the vector orientation of the laser path as opposed to having any link to the layer thickness or layer thickness interface.

4.2. Tensile properties

It is clear the introduction of a joint reduces elongation to failure in the majority of samples. This may raise the point that a (single-layer-thickness) 90 μm layer part is the best option, since these samples exhibit the greatest productivity increase through processing the fewest layers, with no obvious penalty to mechanical response reported in the tensile data. However, mechanical performance is not the only reason one might limit thicker layers to regions of low interest as opposed to an entire part: surface finish, dimensional accuracy and staircasing are all worsened by significantly increasing layer thickness. To maintain higher part quality across various metrics then, it is important to maintain regions of finer layers in areas of high interest; hence interlacing of 30–60 and 30–90 μm layers is deemed valid here despite identical tensile performance of the baseline samples.

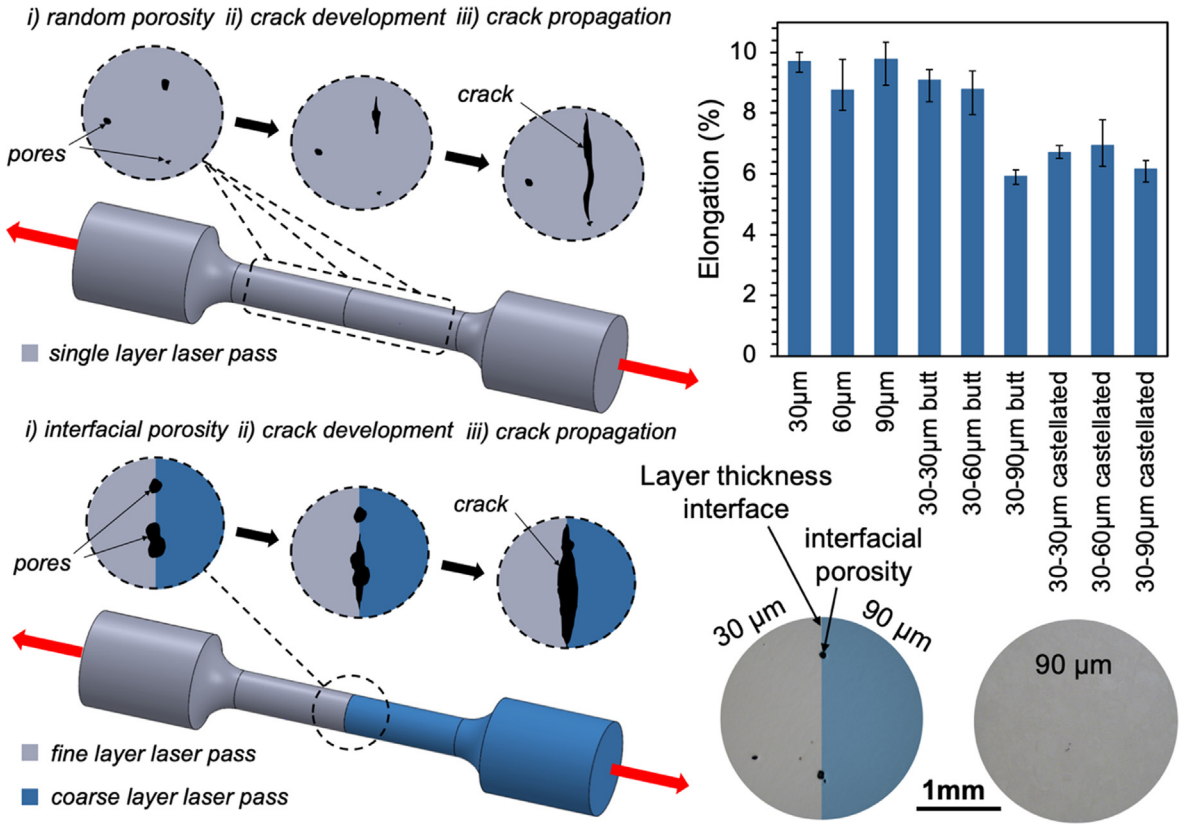

Fig. 9. A schematic to show the role of porosity in failure of samples featuring layer thickness interfaces compared with baseline samples, and the effect on ductility.

The 30–30 μm jointed samples (top-right in Figs. 5 and 6) were manufactured to isolate the introduction of a joint, and hence two parallel regions of one part, as the sole variable. In this way, layer thickness, build parameters and therefore grain structure remains similar either side of the join. Thus, observing any changes in mechanical response within the 30–30 μm jointed sample sets allows one to attribute said changes directly to the union of the two regions, since the bulk material is the same each side of the interface. Since these jointed samples failed exactly at the interface, despite the blending of grain structures at the boundary appearing to be seamless, it is thought that interfacial porosity is the root cause of the premature failure observed in the 30–30 μm castellated joins. By extension, all samples featuring an interface between two regions (30–30, 30–60 or 3–90 μm) likely fail due to interfacial porosity since they fail at the boundary location, however, the 30–30 and 30–60 μm butt jointed samples do not exhibit any penalty to elongation to failure, while the remaining 30–90 μm butt jointed samples and all three castellated samples do. One might anticipate the castellated joints provide a stronger union than butt jointed samples, due to the interlocking geometry increasing the region of blending between the two metal matrices, as was the intention with these designs. Nonetheless, it is hypothesised that, since interfacial porosity is likely the cause of premature failure, the significantly increased area of the castellated interface provides a larger region for defect formation when compared with the butt interface. This greater number of pores lends itself to accelerating crack initiation and propagation to a greater extent. We can therefore propose that interface design requires careful consideration with respect to the mating area between interfaces.

The 30–90 μm samples feature layer thickness boundaries displaying significantly greater interfacial porosity, both in terms of frequency and size as more keyhole pores became evident. Similarly, at 90 μm, these samples were the first to display evidence of an interface in the grain structure (section 3.1), exhibiting poorer fusion between the two regions. This could suggest 90 μm represents a critical layer thickness, at which the two metal matrices begin to show a clear microstructural boundary; this hypothesis may be supported further by the 30–90 μm castellated joins being the only sample set to show any reduction in UTS and yield stress, albeit very minor (1.4% and 1.6% respectively). It is possible that the observed microstructural boundaries have an effect on mechanical response of the joins; nonetheless, the increase in interfacial porosity in the 90 μm sample sets likely dominates failure.

4.3. Fracture behaviour

Fracture surfaces indicative of more brittle failure are evident in the jointed samples as a whole, when compared with baseline samples. Similarly, an increase in layer thickness exhibits even less evidence of plasticity – indicated by flatter and rougher fracture surfaces as the coarser layer regions becomes thicker (30, 60 and 90 μm from left to right columns in Fig. 8). As discussed in the tensile results section of the study (section 3.2), this is attributed to an increased fraction of internal defects at the interface between the two distinct regions of the part, using two parallel laser scan paths.

Simonelli et al. [15] reported that LPBF Ti6Al4V experiences intergranular fracture, owing to weak texture and α-laths arranged with high-angle boundaries. Since these samples were manufactured horizontally on the substrate, they feature large columnar prior-β grains perpendicular to the load direction. While interfacial porosity initiates crack growth in these samples, the crack propagates along the long edge of these prior-β grains (parallel) in the region of the interface. Altering the build orientation to angle the columnar grains will likely affect the failure of these samples. For

example, vertically built samples will feature columnar grains parallel to the gauge length and thus fracture will likely occur perpendicularly through the cross sections of the grains - Fig. 5 shows the direction of the columnar grains relative to the build axes.

5. Conclusions

A novel method to interlace multiple layer thicknesses within single LPBF components has been presented. This study characterises samples featuring a union between finer and coarser layer thickness regions to compare part quality with standard, single-layer thickness parts. This method enables increased build rates as thicker layers require significantly reduced laser-on time, while maintaining finer layers in regions of high interest to preserve part performance for specific load cases. Two interface geometries were examined - a flat surface join, or 'butt' joint, and interlocked teeth, or a 'castellated' joint. The samples were characterised by porosity analysis, microstructural analysis, tensile testing and fractography.

While the findings here have demonstrated the validity of this method, some optimisation of the interfaces between disparate layer thickness regions is necessary, depending on the application. If adopted entirely for increasing throughput, further work is required to improve the fusion between the two regions to reduce interfacial porosity and therefore minimise penalties to mechanical performance. The primary focus for achieving improved fusion is likely through custom laser scan paths, in which a tertiary laser pass may remelt the interface region to eliminate existing pores, the two regions may comprise of one continuous scan path as opposed to two parallel passes, or simply an optimised overlap between the two scan paths, for example. Alternatively, this method may be adopted to tailor localised material properties at the interface, to achieve a desired mechanical response or to guide crack propagation under fatigue and creep conditions. For example, interface geometry can be designed to guide stress out of plane for a given service condition to improve part performance. There exists no one optimal interface geometry, but rather the design of the union must be optimised for each specific load case; for example, more complex load cases than that presented in this study may experience torsion as well as tension, and thus joint geometry will be required to combat sheer as well.

Dependent upon the application, the components investigated in this study may achieve a sufficient tensile response, given that Young's modulus, UTS and yield stress remain comparable across sample sets; however, a reduction in elongation of roughly one third must be tolerated in the 30–90 μm butt joints and all castellated samples when compared with the baseline samples, 30–30 and 30–60 μm butt interfaces. While this response may be tolerable in uniaxial tension, genuine service conditions are likely to exhibit more complex loading and further experiments to investigate sheer would provide useful information.

The conclusions are summarised as:

- Fabrication of components featuring regions of multiple layer thicknesses is possible, and geometry of the interfaces can be used to exploit design freedoms of LPBF.
- This method is capable of significantly reducing laser-scan times as well as manipulating metallurgy to control local part properties. Elongation to failure and UTS could be engineered into a given part.
- Further work is required to minimise interfacial porosity between two disparate layer thickness regions, as well as to tailor geometrical interface design for testing under a more complex load case, conducive to in-service conditions.
- High cycle fatigue testing is required to measure cycles to failure in these parts, since literature has proven the role of porosity in failure is amplified under cyclic loading.

Declaration of Competing Interest

The authors declare that they have no known competing financial interests or personal relationships that could have appeared to influence the work reported in this paper.

Acknowledgements

The authors gratefully acknowledge the support of EPSRC for this project under the support of project EP/S513854/1.

Data Availability

The raw/processed data required to reproduce these findings cannot be shared at this time as the data also forms part of an ongoing study.

References

[1] I. Gibson, D. Rosen, B. Stucker, in: Additive Manufacturing Technologies, Springer New York, New York, NY, 2015, pp. 107–145, https://doi.org/10.1007/978-1-4939-2113-3_5.
[2] C.G. Klingaa, T. Dahmen, S. Baier-Stegmaier, S. Mohanty, J.H. Hattel, Investigation of the roughness variation along the length of LPBF manufactured straight channels, Nondestruct. Test. Eval. 35 (3) (Jul. 2020) 304–314, https://doi.org/10.1080/10589759.2020.1785445.
[3] M.-S. Pham, C. Liu, I. Todd, J. Lertthanasarn, Damage-tolerant architected materials inspired by crystal microstructure, Nature 565 (7739) (Jan. 2019) 305–311, https://doi.org/10.1038/s41586-018-0850-3.
[4] C. Yan, L. Hao, A. Hussein, P. Young, Ti–6Al–4V triply periodic minimal surface structures for bone implants fabricated via selective laser melting, J. Mech. Behav. Biomed. Mater. 51 (Nov. 2015) 61–73, https://doi.org/10.1016/J.JMBBM.2015.06.024.
[5] L.C. Ardila, F. Garciandia, J.B. González-Díaz, P. Álvarez, A. Echeverria, M.M. Petite, R. Deffley, J. Ochoa, Effect of IN718 recycled powder reuse on properties of parts manufactured by means of Selective Laser Melting, Physics Procedia 56 (2014) 99–107, https://doi.org/10.1016/j.phpro.2014.08.152.
[6] R. Acharya, J.A. Sharon, A. Staroselsky, Prediction of microstructure in laser powder bed fusion process, Acta Mater. 124 (Feb. 2017) 360–371, https://doi.org/10.1016/j.actamat.2016.11.018.
[7] H. Gong, K. Rafi, H. Gu, G. D. Janaki Ram, T. Starr, and B. Stucker, "Influence of defects on mechanical properties of Ti-6Al-4V components produced by selective laser melting and electron beam melting," *Mater. Des.*, vol. 86, pp. 545–554, Dec. 2015, doi: 10.1016/j.matdes.2015.07.147.
[8] J.R. Poulin, A. Kreitcberg, P. Terriault, V. Brailovski, Long fatigue crack propagation behavior of laser powder bed-fused inconel 625 with intentionally-seeded porosity, Int. J. Fatigue 127 (Oct. 2019) 144–156, https://doi.org/10.1016/j.ijfatigue.2019.06.008.
[9] B. Zhang, Y. Li, and Q. Bai, "Defect Formation Mechanisms in Selective Laser Melting: A Review," doi: 10.1007/s10033-017-0121-5.
[10] N. Sanaei, A. Fatemi, N. Phan, Defect characteristics and analysis of their variability in metal L-PBF additive manufacturing, Mater. Des. 182 (2019) 108091, https://doi.org/10.1016/j.matdes.2019.108091.
[11] H. Gong, K. Rafi, N. V Karthik, T. Starr, and B. Stucker, "Defect Morphology in Ti-6Al-4V Parts Fabricated by Selective Laser Melting and Electron Beam Melting."
[12] M. Simonelli, C. Tuck, N.T. Aboulkhair, I. Maskery, I. Ashcroft, R.D. Wildman, R. Hague, A Study on the Laser Spatter and the Oxidation Reactions During Selective Laser Melting of 316L Stainless Steel, Al-Si10-Mg, and Ti-6Al-4V, Metall. Mater. Trans. A 46 (9) (2015) 3842–3851, https://doi.org/10.1007/s11661-015-2882-8.
[13] C.M. Cepeda-Jiménez, F. Potenza, E. Magalini, V. Luchin, A. Molinari, M.T. Pérez-Prado, Effect of energy density on the microstructure and texture evolution of Ti-6Al-4V manufactured by laser powder bed fusion, Mater. Charact. 163 (2020) 110238, https://doi.org/10.1016/j.matchar.2020.110238.
[14] T.M. Mower, M.J. Long, Mechanical behavior of additive manufactured, powder-bed laser-fused materials, Mater. Sci. Eng. A 651 (Jan. 2016) 198–213, https://doi.org/10.1016/j.msea.2015.10.068.
[15] M. Simonelli, Y.Y. Tse, C. Tuck, Effect of the build orientation on the mechanical properties and fracture modes of SLM Ti–6Al–4V, Mater. Sci. Eng. A 616 (Oct. 2014) 1–11, https://doi.org/10.1016/J.MSEA.2014.07.086.

[16] Z. Zou, M. Simonelli, J. Katrib, G. Dimitrakis, R. Hague, Refinement of the grain structure of additive manufactured titanium alloys via epitaxial recrystallization enabled by rapid heat treatment, Scr. Mater. 180 (Apr. 2020) 66–70, https://doi.org/10.1016/j.scriptamat.2020.01.027.
[17] X.Y. Zhang, G. Fang, S. Leeflang, A.J. Böttger, A.A. Zadpoor, J. Zhou, Effect of subtransus heat treatment on the microstructure and mechanical properties of additively manufactured Ti-6Al-4V alloy, J. Alloys Compd. 735 (Feb. 2018) 1562–1575, https://doi.org/10.1016/j.jallcom.2017.11.263.
[18] A.M. Khorasani, I. Gibson, M. Goldberg, G. Littlefair, On the role of different annealing heat treatments on mechanical properties and microstructure of selective laser melted and conventional wrought Ti-6Al-4V, Rapid Prototyp. J. 23 (2) (2017) 295–304, https://doi.org/10.1108/RPJ-02-2016-0022.
[19] M. Baumers, P. Dickens, C. Tuck, R. Hague, The cost of additive manufacturing: Machine productivity, economies of scale and technology-push, Technol. Forecast. Soc. Change 102 (Jan. 2016) 193–201, https://doi.org/10.1016/j.techfore.2015.02.015.
[20] N. W. Makoana, I. Yadroitsava, H. Möller, and I. Yadroitsev, "Characterization of 17-4PH Single Tracks Produced at Different Parametric Conditions towards Increased Productivity of LPBF Systems—The Effect of Laser Power and Spot Size Upscaling," *Met. 2018, Vol. 8, Page 475*, vol. 8, no. 7, p. 475, Jun. 2018, doi: 10.3390/MET8070475.
[21] A. Khorasani, I. Gibson, J. K. Veetil, and A. H. Ghasemi, "A review of technological improvements in laser-based powder bed fusion of metal printers," *Int. J. Adv. Manuf. Technol. 2020 1081*, vol. 108, no. 1, pp. 191–209, May 2020, doi: 10.1007/S00170-020-05361-3.
[22] X. Yan, S. Yin, C. Chen, C. Huang, R. Bolot, R. Lupoi, M. Kuang, W. Ma, C. Coddet, H. Liao, M. Liu, Effect of heat treatment on the phase transformation and mechanical properties of Ti6Al4V fabricated by selective laser melting, J. Alloys Compd. 764 (2018) 1056–1071, https://doi.org/10.1016/j.jallcom.2018.06.076.
[23] R. Molaei, A. Fatemi, N. Phan, Significance of hot isostatic pressing (HIP) on multiaxial deformation and fatigue behaviors of additive manufactured Ti-6Al-4V including build orientation and surface roughness effects, Int. J. Fatigue 117 (Dec. 2018) 352–370, https://doi.org/10.1016/J.IJFATIGUE.2018.07.035.
[24] A. Du Plessis, B. Yelamanchi, C. Fischer, J. Miller, C. Beamer, K. Rogers, P. Cortes, J. Els, E. MacDonald, Productivity enhancement of laser powder bed fusion using compensated shelled geometries and hot isostatic pressing, Adv. Ind. Manuf. Eng. 2 (2021) 100031, https://doi.org/10.1016/j.aime.2021.100031.
[25] A.F. de Souza, K.S. Al-Rubaie, S. Marques, B. Zluhan, E.C. Santos, Effect of laser speed, layer thickness, and part position on the mechanical properties of maraging 300 parts manufactured by selective laser melting, Mater. Sci. Eng. A 767 (2019) 138425, https://doi.org/10.1016/j.msea.2019.138425.
[26] H. Ali, H. Ghadbeigi, K. Mumtaz, Processing Parameter Effects on Residual Stress and Mechanical Properties of Selective Laser Melted Ti6Al4V, J. Mater. Eng. Perform. 27 (8) (Aug. 2018) 4059–4068, https://doi.org/10.1007/s11665-018-3477-5.
[27] Q.B. Nguyen, D.N. Luu, S.M.L. Nai, Z. Zhu, Z. Chen, J. Wei, The role of powder layer thickness on the quality of SLM printed parts, Arch. Civ. Mech. Eng. 18 (3) (Jul. 2018) 948–955, https://doi.org/10.1016/j.acme.2018.01.015.
[28] W. Shi, P. Wang, Y. Liu, Y. Hou, G. Han, Properties of 316L formed by a 400 W power laser Selective Laser Melting with 250 μm layer thickness, Powder Technol. 360 (Jan. 2020) 151–164, https://doi.org/10.1016/j.powtec.2019.09.059.
[29] I. Yadroitsev and I. Smurov, "Selective laser melting technology: From the single laser melted track stability to 3D parts of complex shape," in *Physics Procedia*, 2010, vol. 5, no. PART 2, pp. 551–560, doi: 10.1016/j.phpro.2010.08.083.
[30] Charlotte de Formanoir, Umberto Paggi, Thomas Colebrants, Lore Thijs, Guichuan Li, Kim Vanmeensel, Brecht Van Hooreweder, Increasing the productivity of laser powder bed fusion: Influence of the hull-bulk strategy on part quality, microstructure and mechanical performance of Ti-6Al-4V, Addit. Manuf. 33 (2020) 101129, https://doi.org/10.1016/j.addma.2020.101129.
[31] Adam Clare, Alex Gullane, Christopher Hyde, James W. Murray, Simon Sankare, Wessel W. Wits, Interlaced layer thicknesses within single laser powder bed fusion geometries, CIRP Ann. 70 (1) (2021) 203–206, https://doi.org/10.1016/j.cirp.2021.03.001.
[32] Q. Liu, M. Brandt, J. Elambasseril, P. K. Sharp, S. Sun, and R. Djugum, "Mechanical properties of selective laser melted Ti-6Al-4V with different layer thickness," 2018, pp. 819–824, doi: 10.2351/1.5063131.
[33] A.E. Wilson-Heid, Z. Wang, B. McCornac, A.M. Beese, Quantitative relationship between anisotropic strain to failure and grain morphology in additively manufactured Ti-6Al-4V, Mater. Sci. Eng. A 706 (Oct. 2017) 287–294, https://doi.org/10.1016/j.msea.2017.09.017.
[34] Zongyu Xie, Yu Dai, Xiaoqin Ou, Song Ni, Min Song, Effects of selective laser melting build orientations on the microstructure and tensile performance of Ti–6Al–4V alloy, Mater. Sci. Eng. A 776 (2020) 139001, https://doi.org/10.1016/j.msea.2020.139001.
[35] Sheng Cao, Ruikun Chu, Xigen Zhou, Kun Yang, Qingbo Jia, Chao Voon Samuel Lim, Aijun Huang, Xinhua Wu, Role of martensite decomposition in tensile properties of selective laser melted Ti-6Al-4V, J. Alloys Compd. 744 (2018) 357–363, https://doi.org/10.1016/j.jallcom.2018.02.111.
[36] Bo Song, Xiao Zhao, Shuai Li, Changjun Han, Qingsong Wei, Shifeng Wen, Jie Liu, Yusheng Shi, Differences in microstructure and properties between selective laser melting and traditional manufacturing for fabrication of metal parts: A review, Front. Mech. Eng. 10 (2) (2015) 111–125, https://doi.org/10.1007/s11465-015-0341-2.
[37] "ASM Material Data Sheet, Ti6Al4V (Grade 5), Annealed." [Online]. Available: http://asm.matweb.com/search/SpecificMaterial.asp?bassnum=MTP641. [Accessed: 13-Apr-2021].
[38] David Bourell, Jean Pierre Kruth, Ming Leu, Gideon Levy, David Rosen, Allison M. Beese, Adam Clare, Materials for additive manufacturing, CIRP Ann. - Manuf. Technol. 66 (2) (2017) 659–681, https://doi.org/10.1016/j.cirp.2017.05.009.
[39] H.K. Rafi, T.L. Starr, B.E. Stucker, A comparison of the tensile, fatigue, and fracture behavior of Ti-6Al-4V and 15–5 PH stainless steel parts made by selective laser melting, Int. J. Adv. Manuf. Technol. 69 (5–8) (Nov. 2013) 1299–1309, https://doi.org/10.1007/s00170-013-5106-7.
[40] W.E. King, A.T. Anderson, R.M. Ferencz, N.E. Hodge, C. Kamath, S.A. Khairallah, A.M. Rubenchik, Laser powder bed fusion additive manufacturing of metals; physics, computational, and materials challenges, Appl. Phys. Rev. 2 (4) (2015) 041304, https://doi.org/10.1063/1.4937809.
[41] Adam T. Clare, William J. Reynolds, James W. Murray, Nesma T. Aboulkhair, Marco Simonelli, Mark Hardy, David M. Grant, Chris Tuck, Laser calorimetry for assessment of melting behaviour in multi-walled carbon nanotube decorated aluminium by laser powder bed fusion, CIRP Ann. 69 (1) (2020) 197–200, https://doi.org/10.1016/j.cirp.2020.04.053.